

Enhanced permanganate activation by g-C₃N₄ under visible light irradiation: Unraveled mechanism involving Mn(V) and photo-induced electron

Bin Zhang^a, Shuangqing Xia^a, Zhenyi Wang^a, Wenqian Li^a, Boda Li^a, Haochen Zhang^a, Yanjun Xin^b, Kai Wu^c, Jun Ma^a, Xu He^{a,*}

^a State Key Laboratory of Urban Water Resource and Environment, School of Environment, Harbin Institute of Technology, Harbin 150090, China

^b Qingdao Engineering Research Center for Rural Environment, College of Resource and Environment, Qingdao Agricultural University, Qingdao 266109, China

^c Green Living and Innovation Division, Hong Kong Productivity Council, Hong Kong Special Administrative Region of China

ARTICLE INFO

Keywords:

Mn(VII)

g-C₃N₄

Visible light

Mn(V)

Photo-induced electron

ABSTRACT

Permanganate [Mn(VII)] needs to be activated to improve its reactivity towards refractory organic contaminants in practice. Herein, visible light (VL) and graphitic carbon nitride (g-C₃N₄) were introduced to enhance the activation of Mn(VII) for the first time. Sulfamethoxazole (SMX) can be degraded effectively by VL/Mn(VII)/g-C₃N₄ system in neutral and alkaline environments. Different from conventional Mn(VII) activation and photocatalytic processes, the performance of VL/Mn(VII)/g-C₃N₄ system in various real water samples was superior than Milli-Q water. Mn(V) was found to be the dominant active species responsible for SMX degradation. Photo-induced electron (e_{cb}⁻) of g-C₃N₄ under VL irradiation was proved to be the initiator of Mn(VII) activation. Density functional theory calculations revealed the strong affinity of g-C₃N₄ for Mn(VII), which can resist the interference of water substrates on the Mn(VII) activation process by photo-induced e_{cb}⁻. This work deepens the understanding of reactive manganese intermediates in the Mn(VII) activation system.

1. Introduction

Nowadays, an increasing number of emerging refractory contaminants are found in aquatic environments, which pose a threat to human health and ecological environment [1]. Advanced oxidation processes (AOPs) based on chemical oxidants have received a lot of attention due to their effectiveness and stability [2]. Permanganate [Mn(VII)], a promising oxidant, has attracted wide attention in the field of water treatment due to its low cost, chemical stability, and negligible formation of toxic by-products [2–4]. However, the chemical stability of Mn(VII) determines that it can only react with organic compounds containing electron-rich moieties [5], hindering its further application. Therefore, exploring the activation of Mn(VII) is indispensable to enhance its oxidation capacity.

In recent years, numerous studies focusing on the activation of Mn(VII) have been widely reported. Generally, reducing reagents (e.g., bisulfite and benzoquinone) can initiate the activation of Mn(VII) to generate reactive manganese intermediates (RMnS) [6–8]. However, the residual salinity and toxicity risks restrict its practical applications.

Ultraviolet (UV) radiation has been proven to be an effective means of Mn(VII) activation to generate RMnS and hydroxyl radicals (•OH) [5,9], while the UV-based AOPs are often considered to be chemical- and energy-intensive. To avoid huge energy consumption, Yang et al. reported that simulated solar (SS) could accelerate the degradation of contaminants by Mn(VII) [4]. However, the SS/Mn(VII) process still mainly relies on high-energy UV photolysis, but in fact UV light only accounts for 4% of the solar spectrum. Visible light (VL), which accounts for 46% of the solar spectrum [10], is a promising alternative to energy-consuming UV. Zhang et al. revealed that the VL/Mn(VII) system can produce superoxide radicals (O₂⁻) and manganese trivalent [Mn(III)] to promote the degradation of sulfamethazine (SMT) [11]. Given that SMT can also be oxidized by Mn(VII) directly in dark environment, and the performance of photocatalytic systems is generally inhibited in natural water matrix, further exploration and improvement on the VL-based photocatalytic system for Mn(VII) activation are still crucial. In addition, Shen et al. found that the reaction rate of TiO₂/Mn(VII) system for azo dye was improved under simulated solar irradiation [12]. However, TiO₂ has a low utilization rate of sunlight due to the large

* Corresponding author.

E-mail address: hexu@hit.edu.cn (X. He).

<https://doi.org/10.1016/j.apcatb.2024.123861>

Received 12 November 2023; Received in revised form 25 January 2024; Accepted 15 February 2024

Available online 16 February 2024

0926-3373/© 2024 Elsevier B.V. All rights reserved.

band gap (~ 3.2 eV), resulting in a long reaction time [13]. Moreover, the evolution of Mn(VII) and the role of RMnS in the photocatalytic process also need to be further elucidated.

Very recently, Mn(VII) activation by carbon materials have attracted much attention due to their stable structure, affordability and accessibility [2,3,14–16]. However, as two types of widely studied and utilized carbon materials, Mn(VII) activation by biochar is limited by the regeneration of active sites, and Mn(VII) activation by graphite as the mediator for electron transfer is inhibited in neutral and alkaline environments [2,3]. In addition, their effectiveness for Mn(VII) activation in real water has significantly diminished. Different from biochar and graphite, graphitic carbon nitride ($g\text{-C}_3\text{N}_4$), a novel carbon-based two-dimensional semiconductor, can absorb VL to generate high-energy hole–electron pairs [14]. Generally, the contaminant removal in $g\text{-C}_3\text{N}_4$ -based photocatalytic systems mainly relies on superoxide radicals ($\text{O}_2^{\cdot-}$), which are derived from the reduction of dissolved oxygen by photo-induced electron (e_{cb}^-) [17–19]. However, performance of the system for refractory contaminants is restricted due to the relatively low oxidation capacity of $\text{O}_2^{\cdot-}$ (redox potential: -0.33 V vs NHE).

To solve the above challenges, a novel VL/Mn(VII)/ $g\text{-C}_3\text{N}_4$ system was established for the first time in this study, where Mn(VII) was activated by $g\text{-C}_3\text{N}_4$ under VL irradiation. We speculate that photo-induced e_{cb}^- , as the key initiator for $\text{O}_2^{\cdot-}$ formation, can also activate Mn(VII) to generate highly active RMnS for the degradation of refractory contaminants. $g\text{-C}_3\text{N}_4$ was chosen as the donor of photo-induced e_{cb}^- due to its simple synthesis and favorable VL response. Sulfamethoxazole (SMX), which was refractory to Mn(VII) and VL/Mn(VII) systems, was chosen as the target pollutant. Mechanisms for the direct activation of Mn(VII) by photo-induced e_{cb}^- to generate highly reactive Mn(V) was revealed, and the superior performance of VL/Mn(VII)/ $g\text{-C}_3\text{N}_4$ system in real water was demonstrated.

2. Experiments

2.1. Materials

Sulfamethoxazole (SMX, 98.0%), carbamazepine (CBZ, >98.0%), bisphenol A (BPA, >99.0%), 2,4-dichlorophenol (2,4-DCP, >98.0%), sulfamethazine (SMT, 99%) and pyrophosphate (PP) were purchased from Aladdin Reagent Co., Ltd. Potassium permanganate (KMnO_4), urea and hydroxylamine hydrochloride (HA) were purchased from Sino-pharm Chemical Reagent Co., Ltd. Potassium manganate (K_2MnO_4) was purchased from Alfa Aesar Chemical Co., Ltd. Other chemicals are described in Text S1. $g\text{-C}_3\text{N}_4$ was synthesized via urea polycondensation at 550°C for four hours with a heating rate of $5^\circ\text{C}\cdot\text{min}^{-1}$ in a muffle furnace. The micromorphology, and composition of $g\text{-C}_3\text{N}_4$ are presented in Text S2 and Figure S1. Mn(VI) solution was prepared by dissolving K_2MnO_4 in strong alkaline solution [9,20].

2.2. Experimental procedures

As shown in Figure S2, oxidation experiments were conducted in a cylindrical quartz reactor (5.8 cm in inner diameter) equipped with a magnetic stirrer with open air. Specifically, 25 mg of $g\text{-C}_3\text{N}_4$ was added to a 50 mL solution containing 10 mM sodium borate or sodium acetate and 50 μM Mn(VII). Solution pH was controlled using 10 mM sodium acetate for pH 4.0–6.1 or 10 mM borate sodium for 7.0–9.1. Previous reports have confirmed that the effects of sodium acetate and borax buffering are negligible on SMX degradation by Mn(VII) [2,8]. Meanwhile, the pH of solution was adjusted by sulfuric acid or sodium hydroxide before initiating the reaction. The VL source was provided by a 350 W Xenon lamp equipped with a cutoff filter ($\lambda > 400$ nm). The intensity of incident light in the reaction solution was controlled at $100\text{ mW}/\text{cm}^2$ (about one solar intensity). The irradiation spectrum of VL source is shown in Figure S3. The VL source was preheated for 30 min

before initiating the reaction to obtain a stable light output. For sampling, 1 mL of the sample was filtered through a PTFE membrane and quenched with 50 μM of 0.2 M HA at settled intervals.

For nitrogen (N_2) and oxygen (O_2) atmosphere experiments, the reaction was carried out in a closed quartz reactor. Prior to the reaction, the reaction solution was aerated with N_2 and O_2 for half an hour beforehand, and the N_2 or O_2 was continuously pumped during the reaction.

Solution of Mn(III)-PP was prepared by reaction of Mn(II) and Mn(VII) (a molar ratio of Mn(II): Mn(VII) = 4:1) in PP buffer solution. In this study, 50 μM Mn(III)-PP solution was synthesized by adding 40 μM Mn(VII) and 160 μM Mn(II) into 10 mM PP solution, respectively. The solution of MnO_2 [Mn(IV)] was prepared by mixing Mn(VII) and $\text{Na}_2\text{S}_2\text{O}_3$ [8,21]. Specifically, 20 mL Mn(VII) (50 mM) and 1.875 mL $\text{Na}_2\text{S}_2\text{O}_3$ (200 mM) solution were mixed into 1 L Milli-Q water solution. Then, after leaving the mixed solution for 30 min, a stable MnO_2 colloidal solution was formed.

2.3. Analytical methods and characterizations

The radiation intensity and irradiation spectrum of VL source were recorded with fiber optic spectrometer (P4000, CEAULight, China) and fully automatic optical power meter (CEL-NP2000–2A, CEAULight, China), respectively. Details of compound concentrations detection, SMX intermediate products analysis, and electron paramagnetic resonance (EPR) detection technique are provided in Text S3. Characterizations of fresh and used $g\text{-C}_3\text{N}_4$ are described in Text S4. Mn L-edge X-ray absorption spectroscopy (XAS) was recorded by the BL08U1A beamline station of the Shanghai Synchrotron Radiation Facility (SSRF), and the measurement method was the total electronic yield (TEY) mode. The concentrations of Mn(VII) were measured using a UV–vis spectrometer (T6, PERSEE) at 525 nm with 3 cm optical path microcuvette (2.1 mL). UV–visible spectra of VL/Mn(VII)/ $g\text{-C}_3\text{N}_4$ system and various solution samples were recorded by UV–Vis spectrophotometer (DR5000, HACH) at 200–800 nm. Amperometric i-t curve of $g\text{-C}_3\text{N}_4$ loaded onto a glassy carbon electrode ($g\text{-C}_3\text{N}_4\text{-GCE}$) was acquired by CHI 604E electrochemical workstation, and the details are shown in Text S4.

2.4. Computational method

The adsorption energy (E_{ads}) of O_2 and Mn(VII) with $g\text{-C}_3\text{N}_4$ were acquired by the density functional theory (DFT) calculation. The CASTEP package was used for DFT calculations based on the $g\text{-C}_3\text{N}_4$ single layer framework. The calculation condition was in a vacuum area of approximately 16 \AA . This Supercell Lattice parameters setting avoided the interaction of surrounding adjacent layers. MnO_4^- and oxygen (O_2) single molecular were respectively placed on the centers of the six-fold cavity. The calculation results indicated that the optimized model could co-adsorb O_2 molecules and MnO_4^- by the Pauling mode. Therefore, this paper took this model as the research object to conduct first-principles calculations and discussions. The generalized gradient approximation (GGA) with the Perdew-Burke-Ernzerhof (PBE) function were used to calculate the exchange potential and the correlation potential. The convergence standard was $10^{-6}\text{ eV}/\text{atom}$, and the maximum force is less than $0.002\text{ eV}/\text{\AA}$. The energy cutoff was set to be 450 eV. Meanwhile, the DFT-D model was used for van der Waals correction.

3. Results and discussions

3.1. Enhanced SMX degradation in VL/Mn(VII)/ $g\text{-C}_3\text{N}_4$ system

The degradation of SMX in different systems was evaluated. As shown in Fig. 1a, negligible degradation of SMX was observed in Mn(VII), $g\text{-C}_3\text{N}_4$, VL/Mn(VII) and Mn(VII)/ $g\text{-C}_3\text{N}_4$ systems. Mn(VII), as a selective oxidant, is not effective for the oxidation of SMX containing benzene sulfinic and oxazole [3]. The results show that $g\text{-C}_3\text{N}_4$ had no

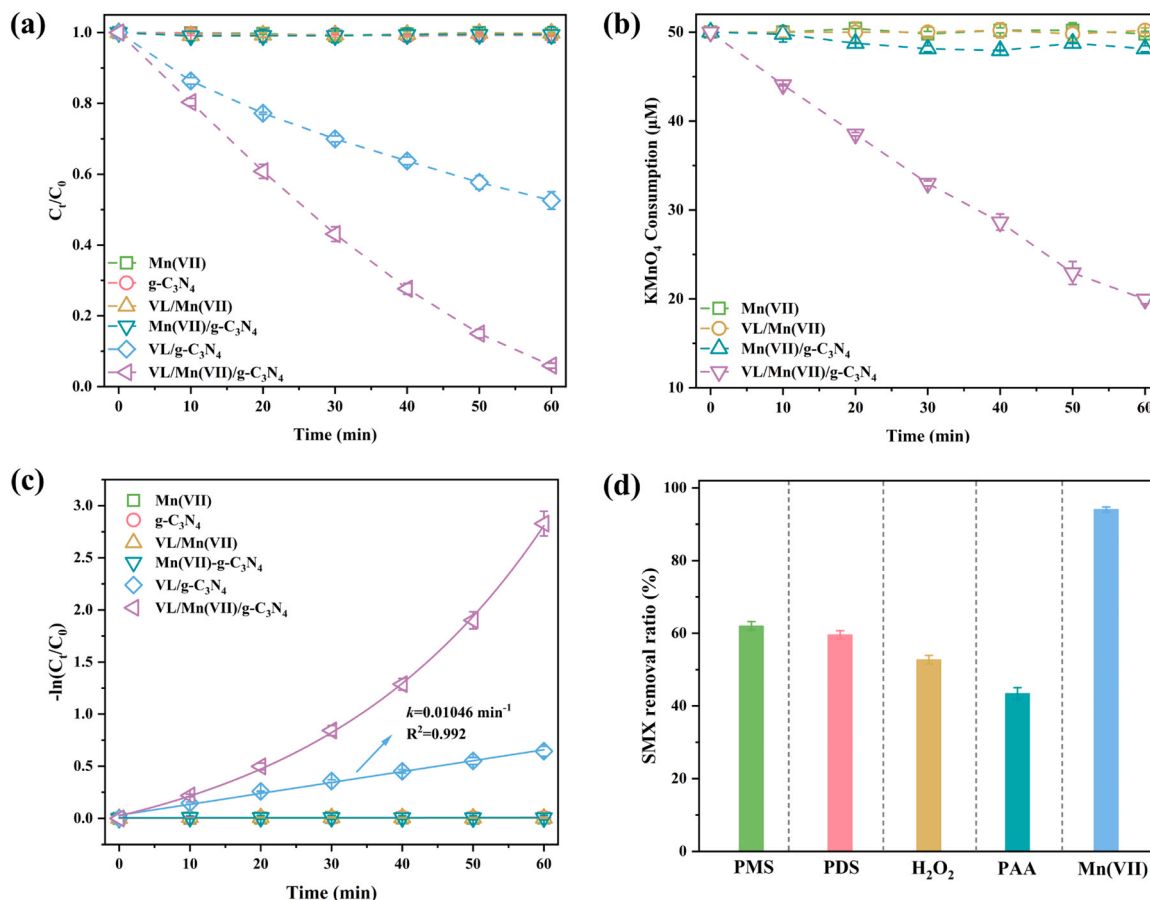


Fig. 1. (a) Degradation of SMX, and (b) concentration changes of Mn(VII) in different systems; (c) $-\ln(C_t/C_0)$ plot of SMX degradation in diverse systems; (d) removal ratio of SMX at 60 min for different oxidation systems. Conditions: $[\text{SMX}]_0 = 10 \text{ μM}$, $[\text{g-C}_3\text{N}_4] = 0.5 \text{ g/L}$, $[\text{Mn(VII)}]_0 = [\text{PMS}]_0 = [\text{PDS}]_0 = [\text{H}_2\text{O}_2]_0 = [\text{PAA}]_0 = 50 \text{ μM}$, and $\text{pH} = 7.0$.

adsorption capacity for SMX, and neither VL nor g-C₃N₄ was effective for Mn(VII) activation. Interestingly, our experimental results are different from the previously reported results that VL can activate Mn(VII) to generate $\text{O}_2^{\cdot-}$ and Mn(III), which may be attributed to the difference in light intensity [11]. Significantly, 0%, 47% and 94% of SMX were degraded by VL/Mn(VII), VL/g-C₃N₄ and VL/Mn(VII)/g-C₃N₄ systems, respectively. In addition, Fig. 1b shows that the consumption of Mn(VII) within 60 min was prominent only in VL/Mn(VII)/g-C₃N₄ system (about 30 μM). These results indicated the addition of g-C₃N₄ greatly improved the oxidation capacity of Mn(VII) for SMX under VL irradiation.

To explore the reaction kinetics of these systems, the relationship between reaction time and $-\ln(C_t/C_0)$ of SMX degradation was investigated in various systems (Fig. 1c). Similar to common AOPs, SMX degradation followed a quasi-first-order kinetics in VL/g-C₃N₄ system. Unexpectedly, the model did not applicable for the VL/Mn(VII)/g-C₃N₄ system. The $-\ln(C_t/C_0)$ of SMX degradation increased gradually faster with the extension of time, which may be related to the reaction mechanism being discussed in the subsequent section. Additionally, SMX degradation in different oxidation systems was also evaluated by replacing Mn(VII) with other oxidants (i.e., PMS, PDS, H₂O₂, and PAA) (Figs. S4a and 4b). In comparison, the removal ratio of SMX by VL/Mn(VII)/g-C₃N₄ system was 32%, 34%, 41%, and 50% higher than that by the VL/PMS/g-C₃N₄, VL/PDS/g-C₃N₄, VL/H₂O₂/g-C₃N₄ and VL/PAA/g-C₃N₄ systems, respectively (Fig. 1d). Moreover, Table S2 presents the SMX degradation in reported heterogeneous Mn(VII) activation systems. Considering the dosage of Mn(VII) and the concentration of SMX, the degradation performance of SMX in VL/Mn(VII)/g-C₃N₄ system is superior to that in most reported Mn(VII) activation systems by other materials. Based on the above analysis, the established VL/Mn(VII)/g-

C₃N₄ system exhibits unique advantages for SMX degradation.

3.2. Identification of reactive species

3.2.1. Probing radicals and $h\nu_{vb}^+$

In general, photocatalytic systems depend primarily on the oxidation capacity of the generated radicals (e.g., $\cdot\text{OH}$ and $\text{O}_2^{\cdot-}$) and photo-induced $h\nu_{vb}^+$ to oxidize target pollutants [14,17,22]. Firstly, the radical signals in different systems were detected through EPR tests using DMPO as a trapping agent. As shown in Fig. 2a, no peaks were detected in Mn(VII), VL/Mn(VII), VL/g-C₃N₄, and VL/Mn(VII)/g-C₃N₄ systems. Tert-butanol (TBA), superoxide dismutase (SOD), and ammonium oxalate (AO) were used as scavengers of $\cdot\text{OH}$, $\text{O}_2^{\cdot-}$, and photo-induced $h\nu_{vb}^+$ [14,23,24], respectively, to further explore the active species in the VL/Mn(VII)/g-C₃N₄ system. Fig. 2b shows that the removal efficiency of SMX was 93%, 92%, and 89% in the presence of 30 mM TBA, 10 KU·L⁻¹ SOD, and 1 mM AO, respectively. The results indicated that the oxidation of SMX by $\cdot\text{OH}$ and $\text{O}_2^{\cdot-}$ in the system was almost negligible. AO only demonstrated slightly inhibitory effects on SMX degradation, indicating that $h\nu_{vb}^+$ are not the dominant oxidizing species in the VL/Mn(VII)/g-C₃N₄ system.

Theoretically, electrons of g-C₃N₄ are transitioned to the conduction band under VL irradiation, leaving photo-induced $h\nu_{vb}^+$ in the valence band (Figs. S5a-5d and Text S5). The oxidation capacity of photo-induced $h\nu_{vb}^+$ from g-C₃N₄ is insufficient to form $\cdot\text{OH}$, due to the lower redox potential of photo-induced $h\nu_{vb}^+$ (+1.96 V vs NHE) than that of $E(\text{H}_2\text{O}_2/\cdot\text{OH}) = +2.34 \text{ V vs NHE}$ and $E(\text{OH}/\cdot\text{OH}) = +1.99 \text{ V vs NHE}$ [25]. Thus, no $\cdot\text{OH}$ is generated in the system. It is worth noting that the potential of photo-induced e_{cb}^- is sufficient to generate $\text{O}_2^{\cdot-}$ ($E(\text{O}_2/\text{O}_2^{\cdot-}) =$

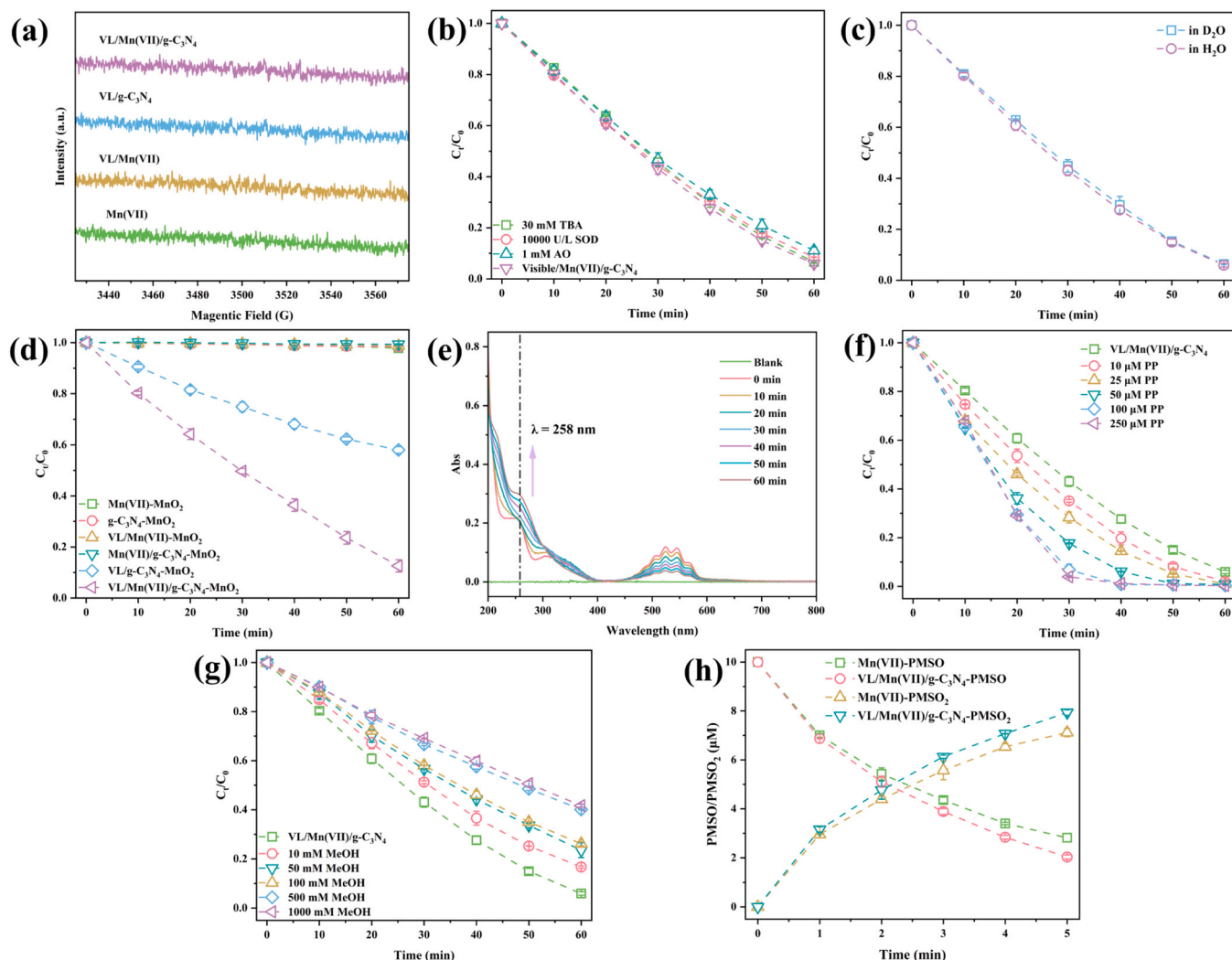


Fig. 2. (a) EPR spectra of various systems with DMPO as trapping agent; (b) effect of TBA, SOD and AO on SMX degradation by the VL/Mn(VII)/g-C₃N₄ system; (c) SMX degradation in the VL/Mn(VII)/g-C₃N₄ system with H₂O and D₂O as solvent; (d) SMX degradation in the presence of 30 μM MnO₂; (e) UV–vis spectra of VL/Mn(VII)/g-C₃N₄ system in the presence of 500 μM PP; (f) effect of PP on SMX degradation by the VL/Mn(VII)/g-C₃N₄ system; (g) SMX degradation by the VL/Mn(VII)/g-C₃N₄ system in the presence of MeOH; (h) PMSO degradation and PMSO₂ generation in various systems. Conditions: [SMX]₀ = 10 μM, [Mn(VII)]₀ = 50 μM, [g-C₃N₄]₀ = 0.5 g/L, and pH = 7.0; (b) [TBA]₀ = 30 mM, [SOD]₀ = 10 KU·L^{−1}, and [AO]₀ = 1 mM; (f) [PP]₀ = 0–250 μM; (h) [MeOH]₀ = 0–1000 mM.

−0.33 V vs NHE) by reacting with dissolved oxygen [25]. However, both EPR tests and quenching experiments have confirmed the negligible role of O₂^{•−}, indicating that the generation path of O₂^{•−} was cut off.

3.2.2. Probing singlet oxygen (¹O₂)

It has been reported that singlet oxygen (¹O₂) can be generated in some photocatalytic systems to degrade contaminants [26–29]. Firstly, EPR experiments were carried out to determine the presence of ¹O₂ in various systems. When TEMP was used as the trapping agent for ¹O₂, the characteristic peaks of 1:1:1 were observed in VL/Mn(VII), VL/g-C₃N₄, and VL/Mn(VII)/g-C₃N₄ systems (Figure S6). Note that the signal intensity of TEMPO (adduct of ¹O₂ and TEMP) in the VL/Mn(VII)/g-C₃N₄ system is weaker than that of VL/Mn(VII) system and far weaker than that of VL/g-C₃N₄ system. In theory, the signal of ¹O₂ in VL/Mn(VII) systems comes from the negligible decomposition of Mn(VII) and excited Mn(VII) under VL irradiation [9]. While, the ¹O₂ in VL/g-C₃N₄ system mainly comes from the reaction of O₂^{•−} with themselves or photo-induced h_ν⁺ [25]. For VL/Mn(VII)/g-C₃N₄ system, the almost undetected O₂^{•−} (as shown in Figs. 2a and 2b) may account for the very weak TEMPO signals. To confirm the role of ¹O₂, the degradation of SMX was investigated in VL/Mn(VII)/g-C₃N₄ system using H₂O and D₂O as solvents,

respectively. Compared to H₂O, D₂O can prolong the lifetime of ¹O₂ due to solvent isotope effect [30]. The physical quenching reaction rate of D₂O for ¹O₂ ($k = 1.6 \times 10^4 \text{ s}^{-1}$) is much lower than that of H₂O ($k = 2.5 \times 10^5 \text{ s}^{-1}$) [31], thus enhancing the oxidation capacity of ¹O₂ towards contaminants. As shown in Fig. 2c, the replacement of solvents did not affect the degradation of SMX, revealing the negligible role of ¹O₂ in the system. Based on the above analysis, it can be concluded that ¹O₂-mediated oxidation can be eliminated in VL/Mn(VII)/g-C₃N₄ system.

3.2.3. Probing reactive manganese species

It has been reported that the formation of RMnS (i.e. Mn(III), Mn(IV), Mn(V), and Mn(VI)) can promote the degradation of organic contaminants in the Mn(VII)-activated system [3,5,7,8,32]. Since Mn(IV) usually exists in the form of manganese dioxide (MnO₂) colloids, the role of Mn(IV) was first investigated. The UV–vis spectrum of synthesized MnO₂ colloid is shown in Figure S7a, and the degradation of SMX by the synthesized Mn(IV) was also investigated. Almost no degradation or adsorption of SMX was observed in 50 μM Mn(IV) solution at pH 7 (Figure S7b). It has been reported that MnO₂ can catalyze Mn(VII) for the oxidation of triclosan and phenolics under slightly acidic conditions

[33]. Thus, MnO_2 colloids were added in various systems to investigate its impact on SMX degradation. Note that the concentrations of added MnO_2 (30 μM) are calculated based on the maximum production from the consumed Mn(VII) in VL/ Mn(VII) /g- C_3N_4 system (Fig. 1b). As depicted in Fig. 2d, for VL/g- C_3N_4 and VL/ Mn(VII) /g- C_3N_4 systems, the degradation efficiency of SMX was reduced by 6% and 5%, respectively, in the presence of 30 μM MnO_2 . The slight inhibition of MnO_2 on the degradation of SMX is mainly attributed to the competitive absorption of VL by MnO_2 . Hence, Mn(IV) was not involved in the degradation process of SMX.

Moving forward to Mn(III) , Jiang et al. reported that it could be chelated by ligand-pyrophosphate (PP) to form Mn(III)-PP complex with the absorption peak at 258 nm [33,34]. The full scan spectra of the reaction solution were performed to identify the presence of Mn(III) during the reaction process. As shown in Fig. 2e, as time extended, the absorption peak at 258 nm increased continuously in VL/ Mn(VII) /g- C_3N_4 solution with 500 μM PP, which could be attributed to the generation of Mn(III) or SMX degradation products. To clarify the dominant one between these two factors, the full spectra changes of the VL/ Mn(VII) /g- C_3N_4 solution in the absence of PP were further tested (Figure S8a). Surprisingly, the absorption peak of 258 nm appeared at 0 min and gradually decreased with the extension of reaction time. Furthermore, the UV–visible spectra of SMX, Mn(VII) , Mn(III)-PP and Mn(VII)+SMX were also recorded separately. Figure S8b shows that the strong absorption peaks at 258 nm can be observed for Mn(III)-PP , SMX and Mn(VII) solutions. Therefore, the absorption peak of 258 nm for VL/ Mn(VII) /g- C_3N_4 solution without PP at 0 min was derived from SMX and Mn(VII) . And the continuous decline of it can be attributed to the degradation of SMX, which also confirmed that there is no absorption peak at 258 nm for SMX degradation products. Therefore, the continuous increase of absorption peak at 258 nm in VL/ Mn(VII) /g- C_3N_4 solution with 500 μM PP was attributed to the formation of Mn(III)-PP . According to the above analysis, there was indeed Mn(III) in the VL/ Mn(VII) /g- C_3N_4 system, and its concentration increased gradually with the extension of reaction time.

To verify the role of Mn(III) , the degradation of SMX was probed by introducing PP into the reaction system. It has been reported that PP can chelate with Mn(III) to form Mn(III)-PP , which may have weak oxidation ability and inhibit the degradation of contaminants [3,11]. Surprisingly, as PP concentration increased from 0 to 250 μM , the degradation process of SMX gradually accelerated (Fig. 2f), suggesting that Mn(III) could not be the main active species responsible for SMX degradation. Furthermore, to determine the role of Mn(III)-PP on SMX degradation, instead of adding PP directly into the VL/ Mn(VII) /g- C_3N_4 system, we synthesized the Mn(III)-PP complex separately and explored its performance for SMX degradation. Detailed procedures for the synthesis of Mn(III)-PP complex and experimental results are provided in Section 2.2 and Figure S9. Experimental results indicated that the synthesized 50 μM Mn(III)-PP complex had negligible reaction activity with SMX (Figure S9). Therefore, although Mn(III) exists in the VL/ Mn(VII) /g- C_3N_4 system, it did not contribute to the degradation of SMX. In addition, the ineffectiveness of active Mn(III) on SMX degradation was also proved by adjusting the dosing sequence of SMX and manganese solution, with specific details in Text S6 and Figure S10. Besides Mn(III) , Yang et al. reported that Mn(V) can also be stabilized by PP, and acknowledged that although Mn(V)-PP is less stable than Mn(III)-PP , it has higher reactive activity than Mn(III) [9]. Thus, the accelerated degradation of SMX by PP implied that Mn(V) may be responsible for the degradation of SMX.

According to the above results, only Mn(V) or Mn(VI) may be responsible for SMX degradation due to the inactivity of Mn(III) and Mn(IV) with SMX. In general, Mn(VI) can only exist stably under strong alkaline conditions, while rapidly disproportionate to generate Mn(V) (Eq. 1) under neutral and acidic conditions [9,35]. To explore the role of Mn(VI) , Mn(VI) was also prepared separately (UV–vis spectrum shown in Figure S11a) and used for SMX degradation. The experimental results

indicated that SMX was inert to Mn(VI) even under strong alkaline conditions (Figure S11b). However, SMX degradation can be observed under neutral conditions by disproportionation of Mn(VI) (Figures S11c and 11d, Text S7), implying that Mn(V) may be a potentially active species.



By excluding the roles of Mn(III) , Mn(IV) and Mn(VI) , it can be speculated that Mn(V) was responsible for the degradation of SMX in the VL/ Mn(VII) /g- C_3N_4 system. Methanol (MeOH) can quench both Mn(V) and $\cdot\text{OH}$ [9,35], however, there are no $\cdot\text{OH}$ in the established system (Figs. 2a and 2b), so MeOH can be selected as the scavenger for Mn(V) in this study. Fig. 2g shows the effects of MeOH with various concentrations on SMX degradation. The addition of MeOH significantly restricted the degradation of SMX by quenching Mn(V) , which confirms the role of Mn(V) for SMX degradation. Furthermore, Mn(V) can accelerate the degradation of methyl phenyl sulfoxide (PMSO) and promote the formation of methyl phenyl sulfone (PMSO_2) [7]. Thus, PMSO was used as a chemical probe to confirm the presence of Mn(V) . As shown in Fig. 2h, the degradation of PMSO and the formation of PMSO_2 in the VL/ Mn(VII) /g- C_3N_4 system were significantly faster than that in the Mn(VII) system. Different from Mn(V) , $\cdot\text{OH}$ react with PMSO to form hydroxylation products instead of PMSO_2 [9]. Thus, there is no prominent difference in the ultimate conversion efficiency of PMSO to PMSO_2 between the VL/ Mn(VII) /g- C_3N_4 ($\eta=99.8\%$) and Mn(VII) ($\eta=99.1\%$) systems, which also revealed the absence of radicals (i.e., $\cdot\text{OH}$) in VL/ Mn(VII) /g- C_3N_4 system. Comparatively, the conversion of PMSO and PMSO_2 was investigated in the VL/g- C_3N_4 system, however, neither the degradation of PMSO nor the generation of PMSO_2 was observed (Figure S12). Therefore, the above results provide tangible evidence for the existence of Mn(V) in the VL/ Mn(VII) /g- C_3N_4 system, which was responsible for SMX degradation.

3.3. Mechanism for Mn(VII) activation

3.3.1. Role of photo-induced electron

Peng et al. reported that graphite can serve as a mediator for direct electron transfer from organics to Mn(VII) [2]. In this study, g- C_3N_4 alone cannot activate Mn(VII) to degrade SMX (Fig. 1a), therefore, the pathway that g- C_3N_4 directly mediates electron transfer to activate Mn(VII) is excluded. Furthermore, due to the fact that Mn(VII) is a stable oxidant, generation of Mn(V) by Mn(VII) activation requires the participation of reducing species, such as O_2^- and photo-induced e_{cb}^- . For VL/ Mn(VII) /g- C_3N_4 system, the role of O_2^- has been excluded by the aforementioned quenching experiments and EPR, so photo-induced e_{cb}^- are considered to be the key initiator for Mn(VII) activation.

Hence, electrochemical method was introduced to provide evidence for Mn(VII) activation by photo-induced e_{cb}^- . The i-t curve of g- C_3N_4 -GCE during the reaction is shown in Fig. 3a. In dark environment, there was initially dark current in the system, but the system tends to stabilize with the extension of time. After stabilization, almost no current was further observed in the dark environment, indicating that there was no electron transfer occurring in the system. This further confirms that there is no electron transfer between g- C_3N_4 and Mn(VII) (or SMX). Then, a noticeable photo-current can be observed by irradiating g- C_3N_4 with VL. When g- C_3N_4 absorbs photons with sufficient energy ($VL < 460 \text{ nm}$), separation of photo-generated electron-hole pairs occurs, and the transfer of photo-electrons further causes the generation of current. Note that a sharp current peak appeared with the injection of Mn(VII) , which could be attributed to the charging current generated by the diffusion of Mn(VII) from the bulk solution to the surface of g- C_3N_4 -GCE [36]. Thereafter, the continuous increase of the current value could be attributed to the current generated by the conversion of Mn(VII) towards the RMnS . Subsequently, the addition of SMX reduced the current value, mainly because the consumption of intermediate RMnS inhibited its transformation and further decreased the expansion of current value.

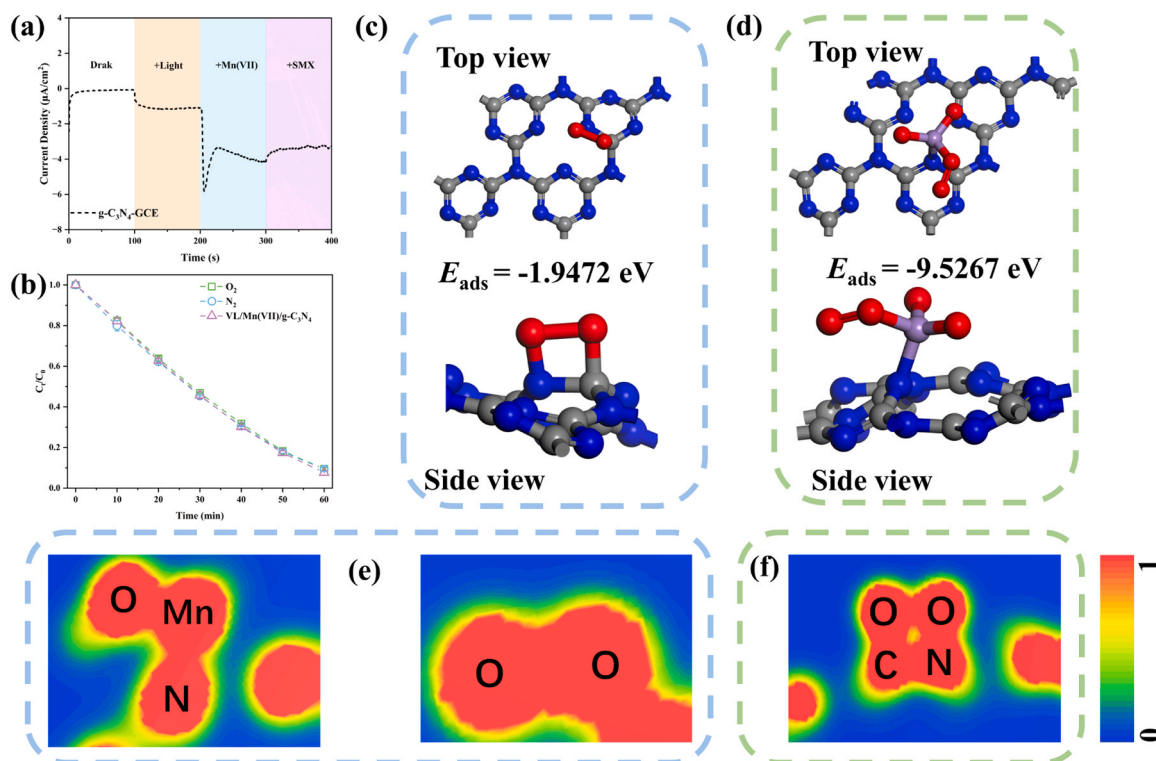


Fig. 3. (a) *I*–*t* curve measurement using g-C₃N₄-GDE as the working electrode; (b) SMX degradation by the VL/Mn(VII)/g-C₃N₄ system at N₂ and O₂ atmosphere; the optimized adsorption structure of (c) O₂ and (d) Mn(VII) on the g-C₃N₄ surface; the electronic cloud distribution map of (e) O₂ and (f) Mn(VII) adsorbed on the g-C₃N₄ surface. Conditions: [SMX]₀ = 10 μM, [Mn(VII)]₀ = 50 μM, [g-C₃N₄] = 0.5 g/L, and pH = 7.0.

Overall, the change of *i*-*t* throughout the entire reaction provides solid evidence for Mn(VII) activation by photo-induced e_{cb}^- .

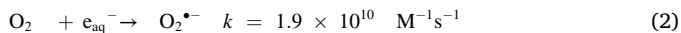


Photo-induced e_{cb}^- can be effectively quenched with dissolved oxygen due to the high reactivity of O₂ and electrons (Eq. 2) [14], thus the role of photo-induced e_{cb}^- was explored by pumping O₂ or N₂ into reaction solution to regulate the concentration of dissolved oxygen (see *Experimental procedures* for details). Surprisingly, the degradation of SMX was affected in neither O₂ nor N₂ atmosphere (Fig. 3b). In order to further reveal the non-effect of increased dissolved oxygen on SMX degradation process, DFT calculation was introduced. Note that N₂ as an inert gas does not normally react with other active species, therefore, only the adsorption energy of O₂ and Mn(VII) for g-C₃N₄ is considered. As shown in Figs. 3c and 3d, the corresponding adsorption energies are −1.95 eV and −9.5 eV, respectively. Detailed energy of substance and Mulliken charge populations of atoms are shown in Table S3 and Figure S13. At the same time, the coincidence of electron clouds between Mn atoms of Mn(VII) and N atoms of g-C₃N₄, and the overlap of electron clouds between O atoms of O₂ and C or N atoms of g-C₃N₄, can also indicate the formation of corresponding adsorption bonds [37]. It is worth noting that the adsorption energy between g-C₃N₄ and Mn(VII) is much higher than that between g-C₃N₄ and O₂. This indicates that when Mn(VII) and O₂ exist simultaneously, the adsorption and exothermic process of Mn(VII) on g-C₃N₄ is more likely to occur than that of O₂ on g-C₃N₄, so Mn(VII) occupies the dominant position in the competitive adsorption on g-C₃N₄. In view of the difficulty of O₂ in accessing g-C₃N₄ surface, it could not quench the photo-induced e_{cb}^- effectively, so the degradation of SMX was not inhibited by increasing the concentration of dissolved oxygen (Fig. 3b). At the same time, the strong adsorption of g-C₃N₄ for Mn(VII) can also improve the utilization of photo-induced e_{cb}^- , which is beneficial for reducing Mn(VII) to RMnS by photo-induced e_{cb}^- . In addition, when

g-C₃N₄ was dispersed in solution containing Mn(VII) for 60 min, the concentration of Mn(VII) decreased by about 2 μM in the dark environment (Figure S14), indicating that Mn(VII) can be adsorbed on the surface of g-C₃N₄ and occupy the active sites of it.

3.3.2. Proposed reaction pathway for RMnS

To better understand the transformation process of Mn(V), g-C₃N₄ powder before and after the reaction was collected and characterized by XAS. Only the used g-C₃N₄ powder shows the characteristic peaks of manganese (Mn) (Figure S15), and the Mn states were simulated using MnO₂ as a Mn⁴⁺ reference and Mn₂O₃ as an HS Mn³⁺ reference [38,39]. As shown in Fig. 4a, 47.7% Mn³⁺ and 52.3% Mn⁴⁺ were found on the surface of the used g-C₃N₄, among which the Mn⁴⁺ belonged to the MnO₂ particles, and the Mn(III) came from the decomposition of Mn(V) [9,40]. Based on the above discussion, possible reaction mechanisms in the VL/Mn(VII)/g-C₃N₄ system are proposed (Fig. 4b). Firstly, the separation of photo-induced electron-hole pairs from g-C₃N₄ occurred under VL irradiation. The photo-induced h_{vb}^+ can oxidize SMX directly, while photo-induced e_{cb}^- tend to combine with Mn(VII), resulting in the generation of Mn(V). Mn(V) possess high reactivity with SMX, thus promoting the degradation of SMX in the VL/Mn(VII)/g-C₃N₄ system. Then, on the one hand, the Mn(V) is converted into Mn(IV) after the reaction with SMX; on the other hand, Mn(V) is decomposed into Mn(III) under the VL irradiation [9,40]. Meanwhile, part of the Mn(III) exists in the form of manganese oxide, and other part of Mn(III) is disproportionated to form Mn(IV) and Mn(II) (Eq. 3) [35]. In addition, as shown in Fig. 1b, the accelerated increase of $-\ln(C_t/C_0)$ with the extending time implied that Mn(VII) can be rapidly converted to Mn(V), and the production rate of Mn(V) is higher than the cumulative consumption rate of it by SMX and its self-decomposition under VL irradiation.



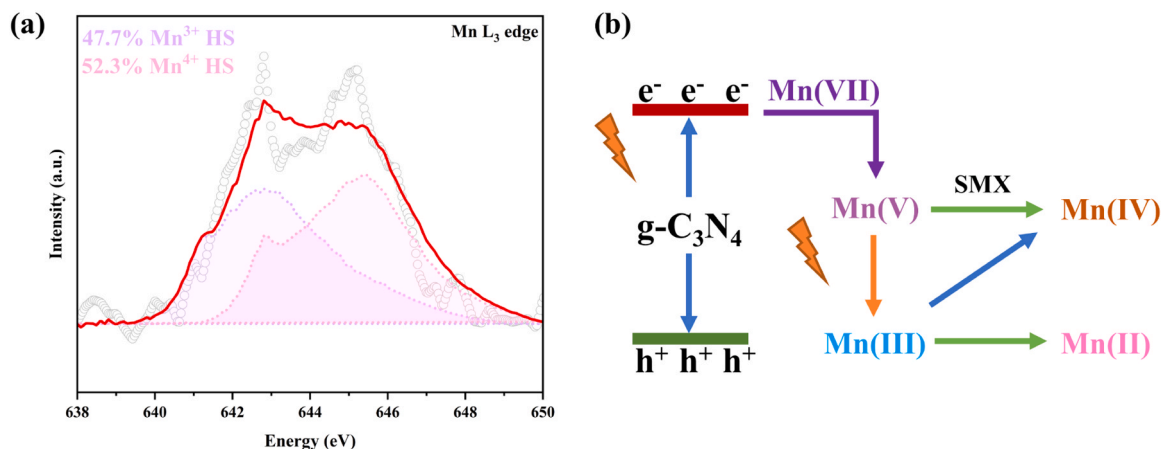


Fig. 4. (a) High resolution Mn L₃ edge XAS spectrum of used g-C₃N₄ and (b) proposed reaction pathway in the VL/Mn(VII)/g-C₃N₄ system.

3.4. Proposed transformation pathways and toxicity evaluation

Twelve intermediates of SMX were identified in the VL/Mn(VII)/g-C₃N₄ system by UPLC-Triple-TOF-MS/MS. Table S4 and Figure S16 listed the twelve identified intermediates of SMX in the VL/Mn(VII)/g-C₃N₄ system, and the proposed transformation pathways are shown in Fig. 5.

Firstly, the amino groups of two SMX molecules can self-couple to

form TP1, which has also been observed in other Mn(VII)-activated systems [2,3]. Meanwhile, SMX was converted into other intermediate products in the VL/Mn(VII)/g-C₃N₄ system through a series of reactions. Specifically, under the action of oxidizing manganese species, the amino group of SMX was converted to nitro group, resulting in the formation of TP5. The amino group of SMX can also be broken to form TP7 by oxidation. Moreover, TP3 can be generated by hydroxylation on the SMX aromatic ring. The amino group of SMX was also easily replaced by

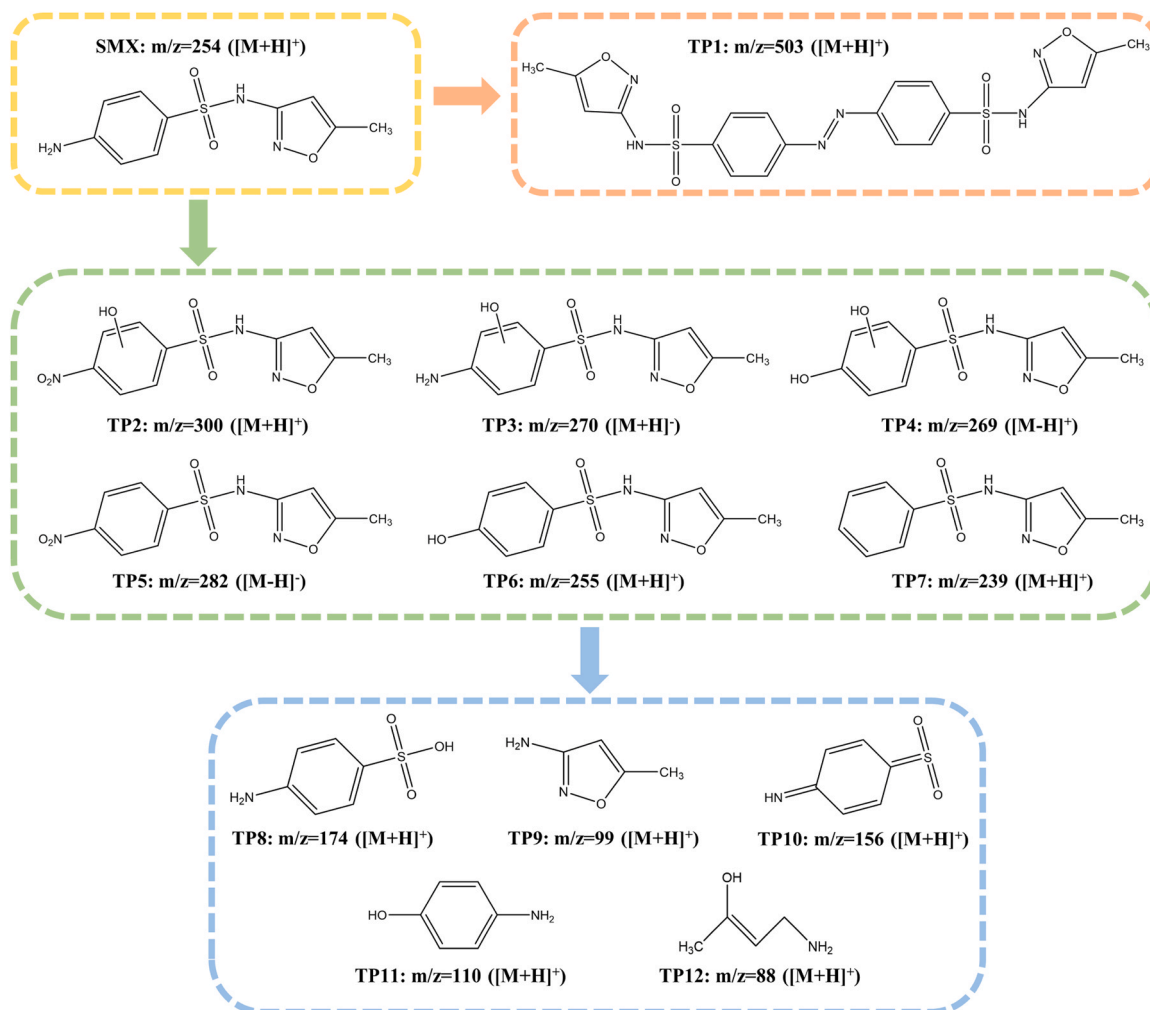


Fig. 5. Transformation pathways of SMX degradation in the VL/Mn(VII)/g-C₃N₄ system.

the hydroxyl group to form TP6 during the electrophilic reaction, and can be further hydroxylated to form TP4. Besides, TP2 can be generated through simultaneous reaction of electrophilic addition and oxidation to SMX. In addition, the hydrolysis of SMX during chemical degradation has also been widely reported [3,41,42]. Similarly, TP8, TP9, and TP11 are the hydrolysis products of the aforementioned intermediates and SMX, respectively. Furthermore, oxidizing species decompose these intermediates into small molecules such as TP10 and TP12.

In addition, the *V. qinghaiensis* Q67 luminescent bacteria were used to evaluate the toxicity of the VL/Mn(VII)/g-C₃N₄ system for SMX degradation. Detailed experimental details are presented in Text S8. The test results of acute toxicity during the reaction are shown in Fig. 6. L represents the luminescent bacteria luminescence value of the samples, and L_0 represents the luminescent bacteria luminescence value of the blank solution (without SMX). Therefore, the acute toxicity can be evaluated by the value of L/L_0 , which is inversely proportional to the acute toxicity. It can be seen that the inhibition rate of SMX on luminescent bacteria can reach 57.8%, indicating that SMX has high acute toxicity. With the extension of reaction time, the luminescence value of luminescent bacteria increased continuously, indicating that the toxicity in the solution was alleviated. In the VL/Mn(VII)/g-C₃N₄ system, the luminescent bacteria inhibition rate of the sample was 34.9% at 60 min, which indicated that the toxicity was reduced by 22.9% compared to the original SMX. In conclusion, the VL/Mn(VII)/g-C₃N₄ system has excellent detoxification ability to water bodies containing toxic contaminants.

3.5. Practical application of VL/Mn(VII)/g-C₃N₄ and effects of water matrix

3.5.1. Application of VL/Mn(VII)/g-C₃N₄ in Real Water

Oxidation of SMX was investigated in various real water samples (Characteristics are shown in Table S5) to evaluate the practical application of the VL/Mn(VII)/g-C₃N₄ system. It can be seen from Fig. 7a that the oxidation of SMX in various real water samples was significantly faster than that in Milli-Q water (MQ). Therefore, the VL/Mn(VII)/g-C₃N₄ system demonstrated strong adaptability to real water and exhibited excellent potential for practical applications.

As two well-known crucial factors that may determine the performance of Mn(VII)-based AOPs, the influences of pH and inorganic ions were studied in detail to better understand the outstanding performance of the VL/Mn(VII)/g-C₃N₄ system in real water samples.

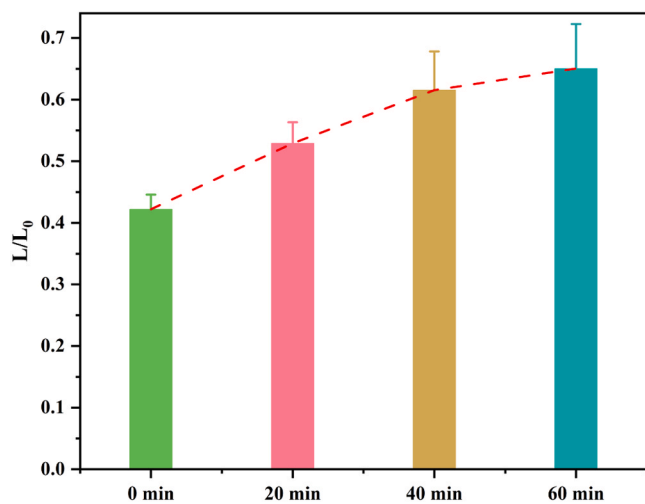


Fig. 6. Variation of *Vibrio qinghaiensis* Q67 luminescence during SMX degradation in the VL/Mn(VII)/g-C₃N₄ system. Conditions: [SMX]₀ = 10 μM, [Mn(VII)]₀ = 50 μM, [g-C₃N₄] = 0.5 g/L, and pH = 7.0.

3.5.2. Effect of pH

Oxidation of SMX in the VL/Mn(VII)/g-C₃N₄ system was further investigated at pH 4.1–9.1. As can be seen, the degradation of SMX was gradually accelerated as pH increased (Fig. 7b). It is worth noting that the degradation of SMX was significantly improved under alkaline condition. For instance, 94.5% and 95.9% of SMX were degraded within 30 min at pH 8.0 and 9.1, respectively. Comparatively, the degradation efficiency of SMX only reached to 43.1% by the VL/Mn(VII)/g-C₃N₄ system within 30 min at pH 4.1. This is mainly because the disproportionation rate of Mn(V) is faster under acidic conditions, whereas it remains more stable under neutral and alkaline conditions [43]. Conclusively, considering the neutral or alkaline condition of natural water, pH can play positive role on the performance of VL/Mn(VII)/g-C₃N₄ in practice.

3.5.3. Effect of inorganic ions

Various inorganic anions exist widely in natural water, and they may react with active species, which can affect the treatment of pollutants by different water treatment processes [9]. Therefore, the effect of representative inorganic anions (i.e., SO₄²⁻, Cl⁻, HCO₃⁻ and NO₃⁻) on the VL/Mn(VII)/g-C₃N₄ system was investigated. As shown in Fig. 7c, almost no changes were observed for SMX degradation in the presence of 5 mM SO₄²⁻, Cl⁻, or NO₃⁻. Interestingly, HCO₃⁻ could greatly accelerate the degradation of SMX in the VL/Mn(VII)/g-C₃N₄ system. The degradation efficiency of SMX could reach 93.6% within only 30 min in the presence of 5 mM HCO₃⁻, which was comparable to its degradation efficiency in MQ water within 60 min. Bisulfite and thiosulfate can stabilize metal ions [Mn(V)] and further promote the degradation of contaminant [1,7,44–46], it is possible that bicarbonate also stabilizes Mn(V) in the VL/Mn(VII)/g-C₃N₄ system. Specifically, HCO₃⁻ can act as a ligand to stabilize Mn(V), which can prevent their disproportionation reaction [1]. As a result, the lifespan of Mn(V) was prolonged, and the exposure time of Mn(V) to react with SMX was increased, thus improving the degradation efficiency of SMX by the VL/Mn(VII)/g-C₃N₄ system.

3.5.4. Applicability of VL/Mn(VII)/g-C₃N₄

Several common contaminants including CBZ, BPA, 2,4-DCP and SMT were also used to evaluate the applicability of the VL/Mn(VII)/g-C₃N₄ system. As shown in Fig. 7d, the degradation rates of CBZ, BPA, 2,4-DCP and SMT were much faster than that of SMX in VL/Mn(VII)/g-C₃N₄ system, indicating its excellent treatment capacity for various types of contaminants. Meanwhile, degradation of other contaminants (i.e., CBZ, BPA, 2,4-DCP and SMT) by different systems is shown in Figure S17. Compared with Mn(VII), VL/Mn(VII) and VL/g-C₃N₄ systems, VL/Mn(VII)/g-C₃N₄ system still exhibited the most prominent degradation ability for other contaminants, which further confirmed the efficient activation of Mn(VII) by g-C₃N₄ under VL irradiation.

3.6. Effect of Mn(VII) and g-C₃N₄ concentrations on SMX removal

The effect of VL/Mn(VII)/g-C₃N₄ system parameters (i.e., Mn(VII) and g-C₃N₄ concentrations) on SMX degradation was further investigated. As shown in Fig. 8a, the degradation efficiency of SMX increased from 77.4% to 95.9% with the Mn(VII) concentration increasing from 0 to 50 μM. This result can be interpreted as follows: more Mn(VII) being activated by photo-induced e_{cb}⁻ with the increase of Mn(VII) concentration, thus generating more active RMnS to degrade SMX. It is worth noting that the degradation efficiency of SMX decreased from 95.9% to 92.5% as the Mn(VII) concentration increased from 50 to 250 μM. This may be attributed to the increased concentration of Mn(VII), which led to an increase in the chroma of reaction solution, hindering the absorption of photocatalyst for VL. Fig. 8b shows the degradation efficiency of SMX at different g-C₃N₄ concentrations. The oxidation efficiency of SMX enhanced from 70.2% to 95.9% within 60 min as the g-C₃N₄ concentrations increasing from 0.1 g/L to 0.5 g/L. When the concentration of g-C₃N₄ was increased from 0.5 g/L to 1 g/L, the

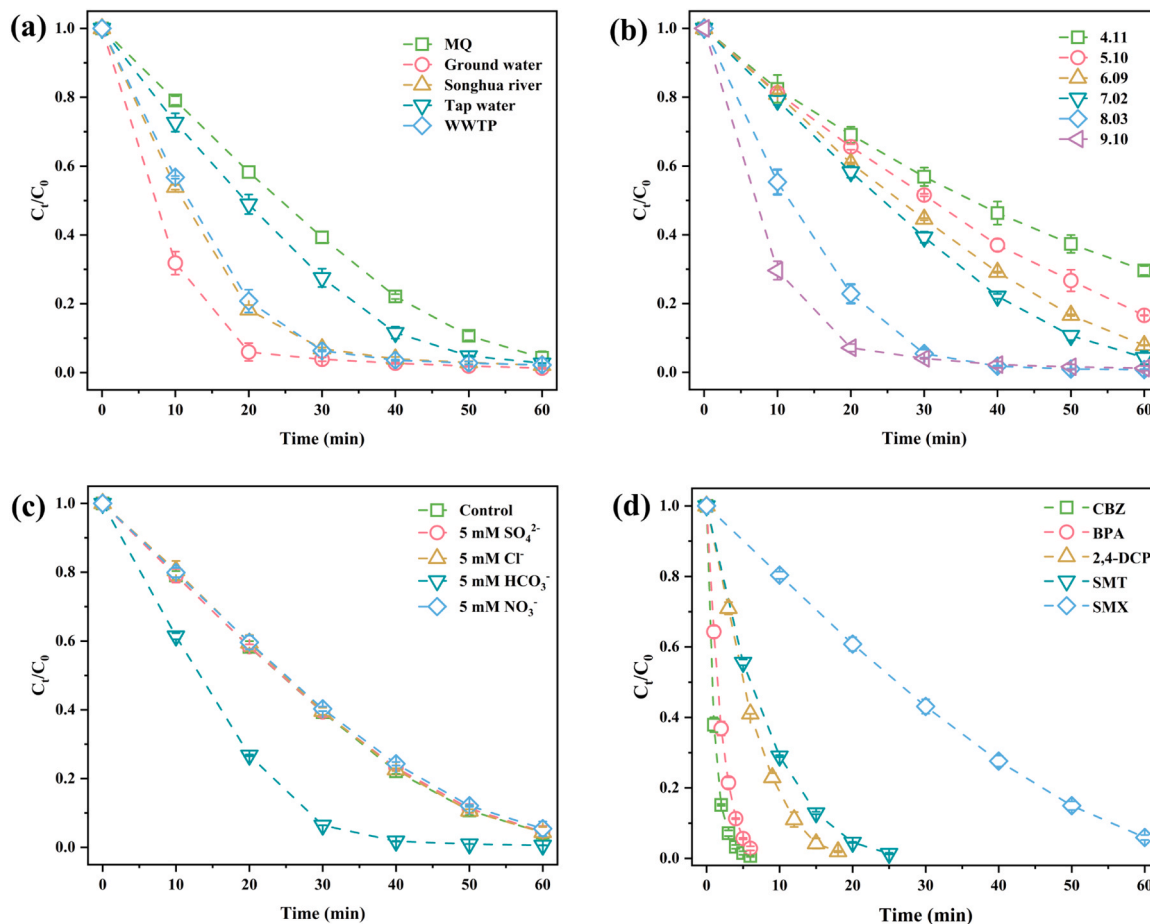


Fig. 7. (a) Degradation of SMX by the VL/Mn(VII)/g-C₃N₄ system in real waters; effect of (b) pH and (c) inorganic ions on SMX degradation by the VL/Mn(VII)/g-C₃N₄ system; (d) degradation of contaminants by the VL/Mn(VII)/g-C₃N₄ system. Conditions: [Mn(VII)]₀ = 50 μM, [g-C₃N₄]₀ = 0.5 g/L, and [CBZ]₀ = [BAP]₀ = [2,4-DCP]₀ = [SMT]₀ = [SMX]₀ = 10 μM; (c)-(d) pH = 7.0.

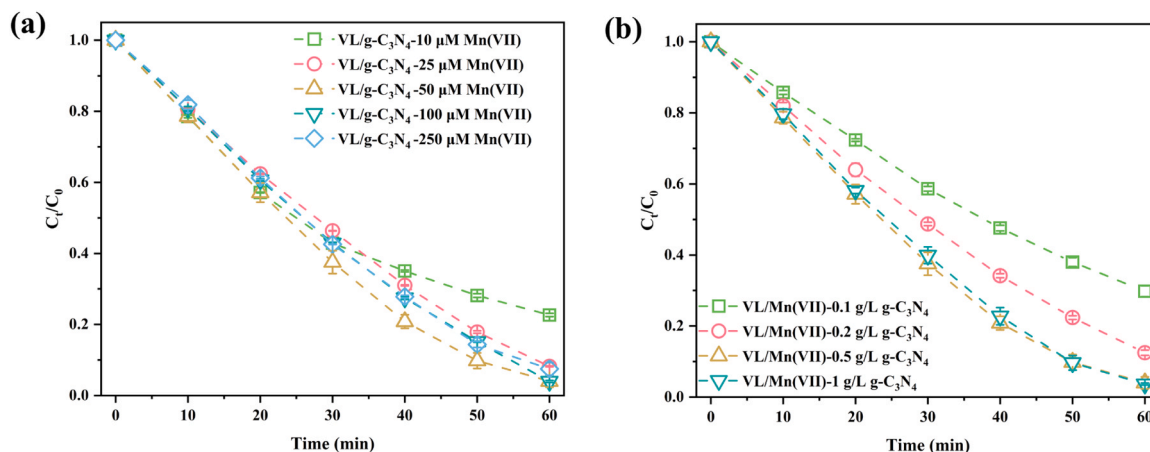


Fig. 8. Effect of (a) Mn(VII) and (b) g-C₃N₄ concentrations on SMX degradation. Conditions: [SMX]₀ = 10 μM, and pH = 7.0; (a) [Mn(VII)]₀ = 0–250 μM, [g-C₃N₄]₀ = 0.5 g/L; and (b) [Mn(VII)]₀ = 50 μM, [g-C₃N₄]₀ = 0–1 g/L.

degradation efficiency of SMX only increased from 95.9% to 96.3%. The increase of g-C₃N₄ concentration can absorb more photon energy to generate photo-induced e_{cb}^- to activate Mn(VII). However, a high concentration of g-C₃N₄ can also hinder the transmission of VL. Therefore, careful consideration of parameters in the VL/Mn(VII)/g-C₃N₄ system is necessary for practical applications.

3.7. Reusability and stability

The reusability of g-C₃N₄ for VL/Mn(VII)/g-C₃N₄ system was evaluated through five cycles. As shown in Fig. 9a, the degradation efficiencies of SMX were 95.3%, 90.4%, 84.7%, 79.0% and 76.1% for the five use cycles of g-C₃N₄. The decline in degradation efficiency can be attributed to the formation of Mn(III) and Mn(IV), which occupy active

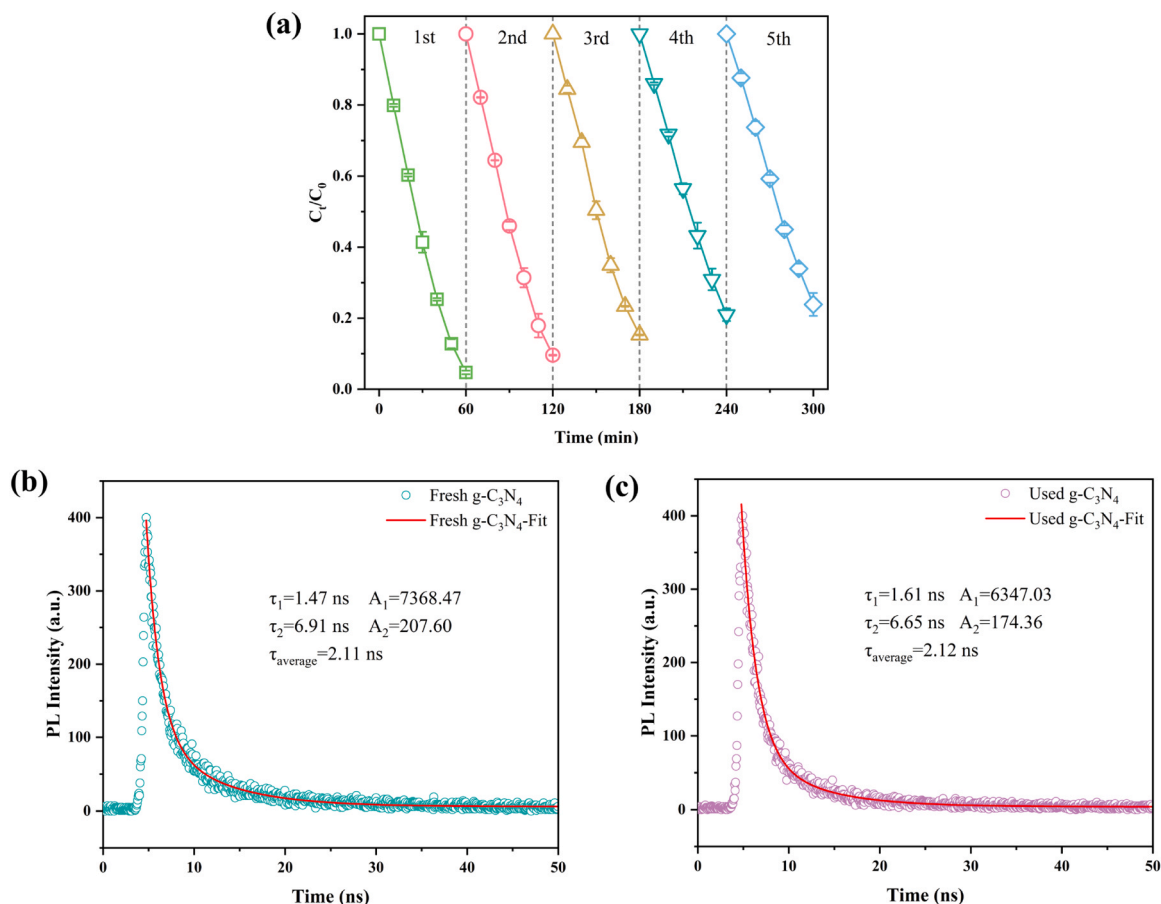


Fig. 9. (a) SMX degradation by the recycling of g-C₃N₄ in the VL/Mn(VII)/g-C₃N₄ system; time-resolved transient PL spectra of (b) fresh and (c) used g-C₃N₄. Conditions: [SMX]₀ = 10 μ M, [Mn(VII)]₀ = 50 μ M, [g-C₃N₄] = 0.5 g/L, and pH = 7.0.

sites on the surface of g-C₃N₄ (Fig. 4a). The MnO₂ particles deposited on the surface of g-C₃N₄ can hinder the absorption of photons, thus reducing the separation of photo-induced carriers. With the decrease of photo-induced e_{cb}^- from photo-induced carriers, the activation efficiency of Mn(VII) gradually decreased. However, it can be seen that SMX degradation by the VL/Mn(VII)/g-C₃N₄ system did not decrease significantly with each recycling. In addition, for deactivated catalysts, we can take ultrasonic or acid heat treatment to remove the deposited Mn(III) and Mn(IV) on the catalyst surface. Furthermore, the time-resolved transient photoluminescence (PL) spectra of fresh and used g-C₃N₄ were recorded. As shown in Figs. 9b and 9c, the time-resolved PL decay curves of fresh and used g-C₃N₄ were determined by double exponential fitting kinetic function (Eq. 4) [47].

$$R(t) = A_1 e^{-t/\tau_1} + A_2 e^{-t/\tau_2} + B \quad (4)$$

$$\tau_{\text{average}} = (A_1 \tau_1^2 + A_2 \tau_2^2) / (A_1 \tau_1 + A_2 \tau_2) \quad (5)$$

where τ_1 and τ_2 are the fast decay component and slow component, A_1 , A_2 and B are constants. Furthermore, the average decay lifetimes (τ_{average}) of fresh and used g-C₃N₄ were calculated by Eq. 5 [47]. The average decay lifetime of used g-C₃N₄ is 2.11 ns, which is comparable to that of fresh g-C₃N₄ (2.12 ns). These results indicated that the lifetime of the photo-induced charge carriers for used g-C₃N₄ was almost not reduced, thus maintaining efficient activation of Mn(VII). Furthermore, the excellent stability of the photocatalyst was also confirmed by XRD, ATR-FTIR, and XPS spectra (Text S9, Figure S18-19).

4. Conclusion

In this study, the initiator (photo-induced e_{cb}^-) of Mn(VII) activation was generated by a easily synthesized photocatalyst under VL irradiation. VL/Mn(VII)/g-C₃N₄ system exhibits the outstanding performance for the degradation of refractory pollutants under neutral and alkaline conditions, the mechanism for efficient activation of Mn(VII) by photo-induced e_{cb}^- to generate active Mn(V) has been revealed. Intriguingly, activation of Mn(VII) by photo-induced e_{cb}^- is not affected by dissolved oxygen due to the strong adsorption capacity of g-C₃N₄ for Mn(VII), so the problem that photo-induced e_{cb}^- are quenched easily in the reaction system can be solved. The system also exhibits strong resistance to inorganic ions, and effectiveness of the system in real water samples has also been verified, indicating its great potential for practical applications. Note that the photocatalyst (g-C₃N₄) used in the system is synthesized without complex modification. Thus, it can provide theoretical guidance for the design of photocatalysts. In addition, Mn(VII) as a solid oxidizer is easier to store and transport than liquid oxidizers such as H₂O₂, chlorine and PAA. Moreover, compared with other AOPs such as persulfate and chlorine systems, problems of byproducts could be avoided in Mn(VII)-based oxidation processes. Although the activation of Mn(VII) by photo-induced e_{cb}^- as initiators provides a novel direction of photocatalyst preparation, however, the knowledge of Mn(V) is extremely limited due to its instability and lack of stable complexing agents. Therefore, future studies are still needed to deepen the exploration of Mn(V).

CRediT authorship contribution statement

Zhang Bin: Conceptualization, Investigation, Methodology, Writing – original draft, Writing – review & editing. **He Xu:** Conceptualization, Funding acquisition, Resources, Supervision, Writing – review & editing. **Ma Jun:** Supervision, Resources. **Wu Kai:** Data curation. **Xin Yanjun:** Resources, Software. **Zhang Haochen:** Formal analysis. **Li Boda:** Data curation. **Li Wenqian:** Software, Formal analysis. **Wang Zhenyi:** Software, Formal analysis. **Xia Shuangqing:** Data curation, Formal analysis.

Declaration of Competing Interest

The authors declare that they have no known competing financial interests or personal relationships that could have appeared to influence the work reported in this paper.

Data availability

Data will be made available on request.

Acknowledgements

This work is supported by the National Natural Science Foundation of China [Grant No. 52000048]; the Natural Science Foundation of Heilongjiang Province [Grant No. YQ2022E030]; State Key Laboratory of Urban Water Resource and Environment (Harbin Institute of Technology) [Grant No. 2023DX15]; Science and Technology Project of Chengde City [202205B008].

Supporting information

The [Supporting Information](#) containing 9 texts, 5 tables, and 19 figures is available online.

Appendix A. Supporting information

Supplementary data associated with this article can be found in the online version at [doi:10.1016/j.apcatb.2024.123861](https://doi.org/10.1016/j.apcatb.2024.123861).

References

- [1] C. Guan, C. Guan, Q. Guo, R. Huang, J. Duan, Z. Wang, X. Wei, J. Jiang, Enhanced oxidation of organic contaminants by Mn(VII) in water, *Water Res.* 226 (2022) 119265.
- [2] J. Peng, P. Zhou, H. Zhou, W. Liu, H. Zhang, C. Zhou, L. Lai, Z. Ao, S. Su, B. Lai, Insights into the electron-transfer mechanism of permanganate activation by graphite for enhanced oxidation of sulfamethoxazole, *Environ. Sci. Technol.* 55 (2021) 9189–9198.
- [3] S.Q. Tian, L. Wang, Y.L. Liu, T. Yang, Z.S. Huang, X.S. Wang, H.Y. He, J. Jiang, J. Ma, Enhanced permanganate oxidation of sulfamethoxazole and removal of dissolved organics with biochar: formation of highly oxidative manganese intermediate species and in situ activation of biochar, *Environ. Sci. Technol.* 53 (2019) 5282–5291.
- [4] T. Yang, J. Mai, S. Wu, W. Luo, M. Zhu, P. Liang, L. Guo, J. Chen, J. Jia, J. Ma, Insight into enhanced activation of permanganate under simulated solar irradiation: rapid formation of manganese species, *Water Res.* 205 (2021) 117669.
- [5] K. Guo, J. Zhang, A. Li, R. Xie, Z. Liang, A. Wang, L. Ling, X. Li, C. Li, J. Fang, Ultraviolet irradiation of permanganate enhanced the oxidation of micropollutants by producing HO[•] and reactive manganese species, *Environ. Sci. Technol. Lett.* 5 (2018) 750–756.
- [6] Z.Y. Dong, Y.L. Lin, T.Y. Zhang, C.Y. Hu, Y. Pan, Z.X. Zheng, Y.L. Tang, B. Xu, N. Y. Gao, Enhanced degradation of emerging contaminants by permanganate/quinone process: case study with bisphenol A, *Water Res.* 219 (2022) 118528.
- [7] Y. Gao, Y. Zhou, S.Y. Pang, J. Jiang, Z. Yang, Y. Shen, Z. Wang, P.X. Wang, L. H. Wang, New insights into the combination of permanganate and bisulfite as a novel advanced oxidation process: importance of high valent manganese-oxo species and sulfate radical, *Environ. Sci. Technol.* 53 (2019) 3689–3696.
- [8] B. Sun, X. Guan, J. Fang, P.G. Tratnyek, Activation of manganese oxidants with bisulfite for enhanced oxidation of organic contaminants: the involvement of Mn(III), *Environ. Sci. Technol.* 49 (2015) 12414–12421.
- [9] T. Yang, J. Mai, M. Zhu, Q. Peng, C. Huang, S. Wu, Q. Tan, J. Jia, J. Fang, J. Ma, Enhanced permanganate activation under UVA-LED irradiation: unraveled mechanism involving manganese species and hydroxyl radical, *Environ. Sci. Technol.* 56 (2022) 17720–17731.
- [10] X.Y. Kong, Y.Y. Choo, S.P. Chai, A.K. Soh, A.R. Mohamed, Oxygen vacancy induced Bi₂WO₆ for the realization of photocatalytic CO₂ reduction over the full solar spectrum: from the UV to the NIR region, *Chem. Commun.* 52 (2016) 14242–14245.
- [11] C. Zhang, S. Tian, F. Qin, Y. Yu, D. Huang, A. Duan, C. Zhou, Y. Yang, W. Wang, Y. Zhou, H. Luo, Catalyst-free activation of permanganate under visible light irradiation for sulfamethazine degradation: experiments and theoretical calculation, *Water Res.* 194 (2021) 116915.
- [12] J. Shen, Z. Jiang, D. Liao, J. Horng, Enhanced synergistic photocatalytic activity of TiO₂/oxidant for azo dye degradation under simulated solar irradiation: a determination of product formation regularity by quantifying hydroxyl radical-reacted efficiency, *J. Water Process Eng.* 40 (2021).
- [13] Y. Tan, Z. Shu, J. Zhou, T. Li, W. Wang, Z. Zhao, One-step synthesis of nanostructured g-C₃N₄/TiO₂ composite for highly enhanced visible-light photocatalytic H₂ evolution, *Appl. Catal. B: Environ.* 230 (2018) 260–268.
- [14] Z. Cheng, L. Ling, Z. Wu, J. Fang, P. Westerhoff, C. Shang, Novel visible light-driven photocatalytic chlorine activation process for carbamazepine degradation in drinking water, *Environ. Sci. Technol.* 54 (2020) 11584–11593.
- [15] S. Xin, S. Huo, C. Zhang, X. Ma, W. Liu, Y. Xin, M. Gao, Coupling nitrogen/oxygen self-doped biomass porous carbon cathode catalyst with CuFeO₂/biochar particle catalyst for the heterogeneous visible-light driven photo-electro-Fenton degradation of tetracycline, *Appl. Catal., B* 305 (2022).
- [16] S. Wang, Y. Wang, S.L. Zhang, S.Q. Zang, X.W.D. Lou, Supporting ultrathin ZnIn₂S₄ nanosheets on Co/N-doped graphitic carbon nanocages for efficient photocatalytic H₂ generation, *Adv. Mater.* 31 (2019) e1903404.
- [17] W. Liu, Y. Li, F. Liu, W. Jiang, D. Zhang, J. Liang, Visible-light-driven photocatalytic degradation of diclofenac by carbon quantum dots modified porous g-C₃N₄: mechanisms, degradation pathway and DFT calculation, *Water Res.* 151 (2019) 8–19.
- [18] S. Wang, Z. Teng, Y. Xu, M. Yuan, Y. Zhong, S. Liu, C. Wang, G. Wang, T. Ohno, Defect as the essential factor in engineering carbon-nitride-based visible-light-driven Z-scheme photocatalyst, *Appl. Catal., B* 260 (2020).
- [19] Y. Wang, H. Wang, F. Chen, F. Cao, X. Zhao, S. Meng, Y. Cui, Facile synthesis of oxygen doped carbon nitride hollow microsphere for photocatalysis, *Appl. Catal., B* 206 (2017) 417–425.
- [20] A. Carrington, M. Symons, 655. Structure and reactivity of the oxy-anions of transition metals. Part I. The manganese oxy-anions, *J. Chem. Soc.* (1956) 3373–3380.
- [21] J.F. Perez-Benito, C. Arias, E. Amat, A kinetic study of the reduction of colloidal manganese dioxide by oxalic acid, *J. Colloid Interface Sci.* 177 (1996) 288–297.
- [22] H.C. Zhang, Y.L. Liu, L. Wang, Z.Y. Li, X.H. Lu, T. Yang, J. Ma, Enhanced radical generation in an ultraviolet/chlorine system through the addition of TiO₂, *Environ. Sci. Technol.* 55 (2021) 11612–11623.
- [23] S. Garg, G. Xing, T.D. Waite, Influence of pH on the kinetics and mechanism of photoreductive dissolution of amorphous iron oxyhydroxide in the presence of natural organic matter: implications to iron bioavailability in surface waters, *Environ. Sci. Technol.* 54 (2020) 6771–6780.
- [24] Y. Yang, Z. Chen, H. Huang, Y. Liu, J. Zou, S. Shen, J. Yan, J. Zhang, Z. Zhuang, Z. Luo, C. Yang, Y. Yu, Z. Zou, Synergistic surface activation during photocatalysis on perovskite derivative sites in heterojunction, *Appl. Catal., B* 323 (2023).
- [25] F. Li, T. Huang, F. Sun, L. Chen, P. Li, F. Shao, X. Yang, W. Liu, Ferric oxide nanoclusters with low-spin Fe(III) anchored g-C₃N₄ rod for boosting photocatalytic activity and degradation of diclofenac in water under solar light, *Appl. Catal., B* 317 (2022).
- [26] L. Xu, L. Li, L. Yu, J.C. Yu, Efficient generation of singlet oxygen on modified g-C₃N₄ photocatalyst for preferential oxidation of targeted organic pollutants, *Chem. Eng. J.* 431 (2022).
- [27] Y. Deng, Z. Zhou, H. Zeng, R. Tang, L. Li, J. Wang, C. Feng, D. Gong, L. Tang, Y. Huang, Phosphorus and potassium co-doped g-C₃N₄ with multiple-locus synergies to degrade atrazine: Insights into the depth analysis of the generation and role of singlet oxygen, *Appl. Catal., B* 320 (2023).
- [28] Q. Sun, X. Wang, Y. Liu, Y. Zhang, S. Xia, J. Zhao, Visible-light-driven g-C₃N₄ doped CuFe₂O₄ floating catalyst enhanced peroxymonosulfate activation for sulfamethazine removal via singlet oxygen and high-valent metal-oxo species, *Chem. Eng. J.* 455 (2023).
- [29] H.B. Truong, S. Bae, J. Cho, J. Hur, Advances in application of g-C₃N₄-based materials for treatment of polluted water and wastewater via activation of oxidants and photoelectrocatalysis: a comprehensive review, *Chemosphere* 286 (2022) 131737.
- [30] P. Shao, Y. Jing, X. Duan, H. Lin, L. Yang, W. Ren, F. Deng, B. Li, X. Luo, S. Wang, Revisiting the graphitized nanodiamond-mediated activation of peroxymonosulfate: singlet oxygenation versus electron transfer, *Environ. Sci. Technol.* 55 (2021) 16078–16087.
- [31] J.D. J.F. Lee, J.B. Hughes, J.H. Kim, Photochemical production of reactive oxygen species by C₆₀ in the aqueous phase during UV irradiation, *Environ. Sci. Technol.* 41 (2007) 2529–2535.
- [32] J. Chen, D. Rao, H. Dong, B. Sun, B. Shao, G. Cao, X. Guan, The role of active manganese species and free radicals in permanganate/bisulfite process, *J. Hazard. Mater.* 388 (2020) 121735.
- [33] J. Jiang, S.-Y. Pang, J. Ma, Oxidation of triclosan by permanganate (Mn(VII)): importance of ligands and in situ formed manganese oxides, *Environ. Sci. Technol.* 43 (2009) 8326–8331.
- [34] J. Jiang, S.-Y. Pang, J. Ma, Role of ligands in permanganate oxidation of organics, *Environ. Sci. Technol.* 2010 (2010) 4270–4275.

- [35] J. Chen, B. Sun, Y. Zhu, Y. Yang, X. Guan, Unraveling the role of Mn(VI) and Mn(V) species in contaminant abatement by permanganate, *Environ. Sci. Technol. Lett.* 9 (2022) 446–451.
- [36] Z. Chen, L. Ryzhik, D. Palanker, Current distribution on capacitive electrode-electrolyte interfaces, *Phys. Rev. Appl.* 13 (2020).
- [37] X. Yang, D. Zhao, First principles study on modification of Ni composite SWCNT material system for gas adsorption, *Appl. Surf. Sci.* 544 (2021).
- [38] J.-H. Cheng, C.-J. Pan, J.-F. Lee, J.-M. Chen, M. Guignard, C. Delmas, D. Carlier, B.-J. Hwang, Simultaneous reduction of Co^{3+} and Mn^{4+} in $\text{P2-Na}_{2/3}\text{Co}_{2/3}\text{Mn}_{1/3}\text{O}_2$ as evidenced by x-ray absorption spectroscopy during electrochemical sodium intercalation, *Chem. Mater.* 26 (2014) 1219–1225.
- [39] M. Risch, K.A. Stoerzinger, B. Han, T.Z. Regier, D. Peak, S.Y. Sayed, C. Wei, Z. Xu, Y. Shao-Horn, Redox processes of manganese oxide in catalyzing oxygen evolution and reduction: an in situ soft x-ray absorption spectroscopy, *Study, J. Phys. Chem. C* 121 (2017) 17682–17692.
- [40] D.G. Lee, C.R. Moylan, T. Hayashi, J.I. Brauman, Photochemistry of aqueous permanganate ion, *J. Am. Chem. Soc.* 109 (1987) 3003–3010.
- [41] L. Hu, P.M. Flanders, P.L. Miller, T.J. Strathmann, Oxidation of sulfamethoxazole and related antimicrobial agents by TiO_2 photocatalysis, *Water Res* 41 (2007) 2612–2626.
- [42] S. Gao, Z. Zhao, Y. Xu, J. Tian, H. Qi, W. Lin, F. Cui, Oxidation of sulfamethoxazole (SMX) by chlorine, ozone and permanganate—a comparative study, *J. Hazard Mater.* 274 (2014) 258–269.
- [43] K. Guo, W. Wei, S. Wu, W. Song, J. Fang, Abatement of structurally diverse micropollutants by the UV/permanganate process: roles of hydroxyl radicals and reactive manganese species, *ACS EST Water* 2 (2022) 593–603.
- [44] D.E. Wilson, Surface and complexation effects on the rate of Mn(II) oxidation in natural waters, *Geochim. Et. Cosmochim. Acta* 44 (1980) 1311–1317.
- [45] B.S. Mandimutsira, B. Ramdhanie, R.C. Todd, H. Wang, A.A. Zareba, R. S. Czernuszewicz, D.P. Goldberg, A. Stable, Manganese(V)-oxo corrolazine, *Complex, J. Am. Chem. Soc.* 124 (2002) 15170–15171.
- [46] Y. Song, J. Jiang, J. Ma, S.-Y. Pang, C. Luo, W. Qin, Oxidation of inorganic compounds by aqueous permanganate: Kinetics and initial electron transfer steps, *Sep. Purif. Technol.* 183 (2017) 350–357.
- [47] P. Wang, S. Zhan, H. Wang, Y. Xia, Q. Hou, Q. Zhou, Y. Li, R.R. Kumar, Cobalt phosphide nanowires as efficient co-catalyst for photocatalytic hydrogen evolution over $\text{Zn}_{0.5}\text{Cd}_{0.5}\text{S}$, *Appl. Catal., B* 230 (2018) 210–219.